InP/GaInP nanowire tunnel diodes

Zeng, Xulu; Otnes, Gaute; Heurlin, Magnus; Mourão, Renato T.; Borgström, Magnus T.

Published in:
Nano Research

DOI:
10.1007/s12274-017-1877-8

2018

Document Version:
Peer reviewed version (aka post-print)

InP/GaInP Nanowire Tunnel Diodes

TABLE OF CONTENTS (TOC)

InP/GaInP Nanowire Tunnel Diodes for Tandem Junction Solar Cell

Xulu Zeng[1], Gaute Otnes[1], Magnus Heurlin[1,2], Renato T Mourão[3], Magnus T Borgström[1,*]

[1]Solid State Physics, NanoLund, Department of Physics, Lund University, P.O. Box 118, SE-22100 Lund, Sweden

[2]Sol Voltaics AB, Ideon Science Park, Scheelevägen 17, SE-22370 Lund, Sweden

[3]Instituto de Física, Universidade Federal do Rio de Janeiro, Caixa Postal 68528, 21941-972 Rio de Janeiro, Brazil

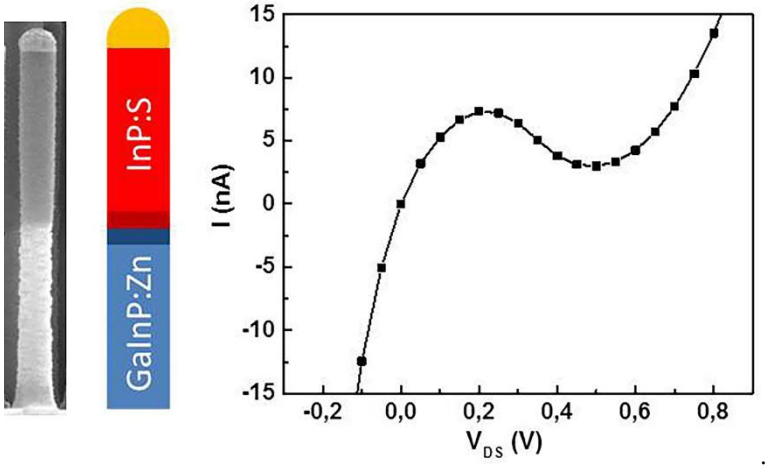

We report the first demonstration of InP/GaInP nanowire tunnel diodes. The realization of nanowire tunnel diodes in both InP/GaInP and GaInP/InP configurations open up an opportunity for nanowire tandem solar cells independent of the growth order of the different materials, opening up for flexibility regarding dopant incorporation polarity.

Provide the authors' webside if possible.

Xulu Zeng, http://www.nano.lu.se/xulu.zeng

Gaute Otnes, http://www.nano.lu.se/tibet/template/Index.vm?pageId=246657

Magnus T Borgström, http://www.nano.lu.se/magnus.borgstrom

InP/GaInP Nanowire Tunnel Diodes

Xulu Zeng[1] (✉), Gaute Otnes[1], Magnus Heurlin[1,2], Renato T Mourão[3], Magnus T Borgström[1]

[1]*Solid State Physics, NanoLund, Department of Physics, Lund University, P.O. Box 118, SE-22100 Lund, Sweden*
[2]*Present address: Sol Voltaics AB, Ideon Science Park, Scheelevägen 17, SE-22370 Lund, Sweden*
[3]*Instituto de Física, Universidade Federal do Rio de Janeiro, Caixa Postal 68528, 21941-972 Rio de Janeiro, Brazil*

ABSTRACT

Semiconductor nanowire solar cells with single p-n junction have achieved comparable efficiency to their planar counterparts with substantial reduction of material consumption. Tandem geometry is a path towards even higher efficiency, for which a key step towards realizing such a device is the fabrication of tunnel (Esaki) diodes within nanowires with correct diameter, pitch, and material combination for maximized efficiency. We have fabricated, characterized and compared the electrical characteristics and material properties of InP/GaInP and GaInP/InP nanowire tunnel diodes with band gap combinations corresponding to high efficiency solar energy harvesting. Four different configurations with respect to material composition and doping were investigated. The nanowire arrays were grown with Metal Organic Vapor Phase Epitaxy from Au particles defined by use of nano imprint lithography, metal evaporation and lift-off. Electrical measurements show that the NWs behave as tunnel diodes in both InP (bottom)/GaInP (top) and GaInP (bottom)/InP (top) configurations, exhibiting a maximum peak current density of 25 A/cm^2, and maximum peak to valley current ratio of 2.5 at room temperature. The realization of NW tunnel diodes in both InP/GaInP and GaInP/InP configurations open up an opportunity for NW tandem solar cells independent of the growth order of the different materials, opening up for flexibility regarding dopant incorporation polarity.

KEYWORDS

nanowire, tunnel diode, InP, GaInP, tandem junction solar cell

1. Introduction

Since the pioneering work by Hiruma in the 1990s [1], there have been considerable progress in III-V semiconductor nanowire (NW) electronic and optoelectronic devices from proof-of-concept towards large scale applications [2-4], NW solar cells have shown great potential to meet the demand of both high efficiency and low cost, with advantages of significant reduction of material consumption, enhancement of light absorption [5] and ease of the constraints of lattice matching [6]. The energy conversion efficiency of NW solar cells is rising rapidly [7]; one of the main parameters considered is the axial junction geometry that significantly affects the device performance [8-10]. The NW devices can be successfully fabricated by vapor-liquid-solid (VLS) growth with desirable crystal quality and optoelectronic properties. To surpass single junction performance limitations, a tandem (multi-junction) geometry can be used [7, 11]. Voltage addition has been observed in InP and

Address correspondence to xulu.zeng@ftf.lth.se

Si single NW [12, 13] and GaAs-NW-array-on-Si tandem solar cell [14]. However, large active areas are necessary for solar cells [15], and an optimal combination of heterostructure materials is needed to match the solar spectra for high solar energy harvesting efficiency. Theoretical calculations solving the full three dimensional Maxwell equations for absorption in an InP/$Ga_{0.3}In_{0.7}P$ NW tandem cell predict a maximum efficiency of 38.5% (with different NW diameter optimized for each subcell) or 35.5% (with uniform NW diameter for all subcells) [16].

A critical component in tandem junction solar cells is the tunnel diode which has been extensively investigated since its invention by Leo Esaki in 1958 [17]. Tunnel diodes function as series connections between pn-junction segments with different band gaps for absorbing different parts of the solar spectrum [18]. To date, NW tunnel diodes have been demonstrated using combinations of binary materials with suggested application in solar cells and electronic devices such as tunneling SRAMs and tunnel FETs [12, 19-24]. However, NW tunnel diodes with material combinations optimal for solar energy harvesting have not been reported.

We manufactured and characterized NW tunnel diodes using the InP/$Ga_{0.3}In_{0.7}P$ material system which has a type I band alignment and the band gaps are given by 1.35 eV and 1.70 eV respectively (an energy band diagram scheme is shown in Fig. S1 in the Electronic Supplementary Material (ESM)). Both types of heterostructures, one with the higher band gap on top (i.e. InP (bottom) / GaInP (top)) and the other with the lower band gap on top (i.e. GaInP (bottom) / InP (top)) were grown and characterized with the purpose of comparing their relative benefits and promise for incorporation as active parts in tandem solar cells. Note that NWs grown with the lower band gap on top will have to be removed from the substrate and processed such that the high band gap junction faces the sun for efficient solar energy harvesting. From these investigations we demonstrated that the efficiency of tunnel diodes independent of doping polarity in the InP/$Ga_{0.3}In_{0.7}P$ material system.

2. Methods

2.1 Growth

Samples were grown in a low-pressure (100 mbar) MOVPE system (Aixtron 200/4) with a total flow of 13 l/min using hydrogen as carrier gas. InP:Zn (111)B substrates were prepared by depositing arrays of Au discs with a diameter of 200 nm, a pitch of 500 nm and height of 65 nm, in a hexagonal pattern by use of nano imprint lithography (NIL), metal evaporation and lift-off [25]. Trimethylindium (TMIn), trimethylgalium (TMGa), phosphine (PH_3), diethylzinc (DEZn), tetraethyltin (TESn), and hydrogen sulfide (H_2S) were used as precursors. Dopant flows for degenerate doping were modulated according to our previous studies of doping evaluation on InP and GaInP NWs [26-29]. The total NW length was 2 µm with each segment of 1 µm, mimicking the position of the tunnel diode in a proposed tandem solar cell structure. The NW length was continuously monitored and controlled in situ by use of reflectance spectroscopy [29, 30]. To improve pattern preservation, a pre-anneal nucleation of InP was implemented at 280 °C for 1 min at TMIn and PH_3 molar fractions of $\chi_{TMIn} = 8.9 \times 10^{-5}$, and $\chi_{PH3} = 6.92 \times 10^{-3}$ [25]. The samples were then heated to an elevated temperature of 550 °C for 10 min under mixed PH_3/H_2 atmosphere to desorb surface oxides, after which the temperature was set to 440 °C. After a minute of temperature stabilization upon reaching 440 °C, growth was initiated by adding TMIn to the precursor flow. First, a 120-nm-long InP stub was grown, with $\chi_{TMIn} = 8.9 \times 10^{-5}$, and $\chi_{PH3} = 6.92 \times 10^{-3}$ respectively. To avoid any radial growth, hydrogen chloride (HCl) was introduced ($\chi_{HCl} = 4.6 \times 10^{-5}$) after 15 s of the InP stub growth [31, 32]. A series of samples with four

different configurations were grown, as listed in Table 1. The GaInP segment was grown with: χ_{TMIn} = 5.2 × 10^{-5}, χ_{TMGa} = 3.96 × 10^{-4}, χ_{PH3} = 6.92 × 10^{-3}, and χ_{HCl} = 5.4 × 10^{-5} for all samples; For the InP segment: χ_{TMIn} = 4.5 × 10^{-5}, χ_{PH3} = 6.92 × 10^{-3}, and χ_{HCl} = 4.6 × 10^{-5} were used.

Table 1 Dopant molar fractions for different configurations

Configurations*	χDEZn	χTESn	χH_2S
InP:Sn/GaInP:Zn	High flow: 1.17 × 10^{-4} Low flow: 8.3 × 10^{-5}	5.6 × 10^{-5}	-
GaInP:Zn/InP:S	High flow: 1.17 × 10^{-4} Low flow: 8.3 × 10^{-5}	-	High flow: 1.6 × 10^{-5} Low flow: 2 × 10^{-6}
InP:S/GaInP:Zn	High flow: 1.17 × 10^{-4} Low flow: 8.3 × 10^{-5}	-	3.1 × 10^{-5}
GaInP:Zn/InP:Sn	High flow: 1.17 × 10^{-4} Low flow: 8.3 × 10^{-5}	5.6 × 10^{-5}	-

*Bold and Italic configurations are the configurations working as tunnel diodes.

Figure 1 exemplifies the precursor flow switching scheme for the InP:Sn/GaInP:Zn (in the following text, working Esaki tunneling configurations are presented in bold and italic for clarity) and GaInP:Zn/InP:S configuration. In order to maximize the p-type doping at the heterojunction, the DEZn flow was kept at χ_{DEZn} = 1.17×10^{-4} ("High flow" in Table 1) for 15 s close to the heterojunction, after/before which it was linearly decreased/ increased for 10 s to/from χ_{DEZn} = 8.3×10^{-5} ("Low flow" in table 1). For the GaInP:Zn/InP:S configuration, the H_2S flow was ramped down to the low flow after 15 s growth of n-type InP segment with high H_2S flow, since we observed that keeping the high doping throughout the segment led to NWs kinking. For the use of TESn, which does not affect the growth dynamics [27], a constant n-type dopant flow was used. The total length of the high doping region close to the heterojunction was approximately 30 nm, measured by in situ reflectance spectroscopy [30].

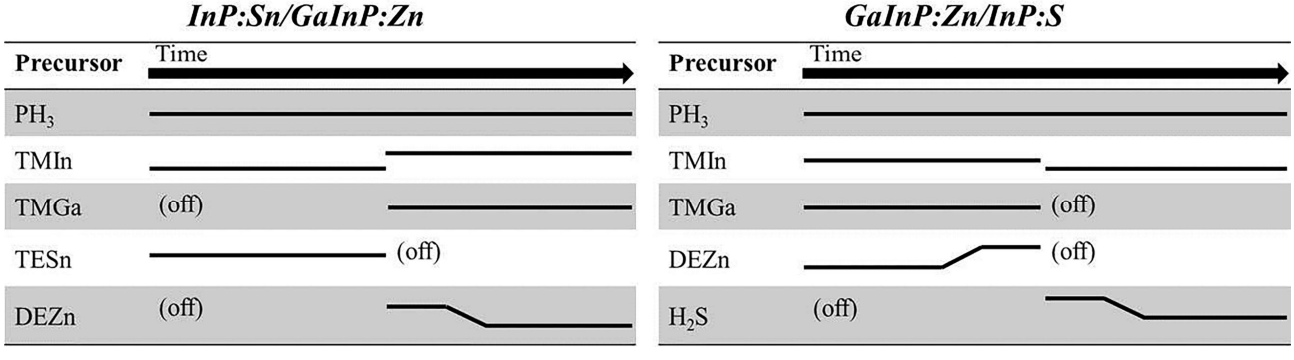

Figure 1 Switching schemes of source flows for the different working configurations, Left: the ***InP:Sn/GaInP:Zn*** configuration; Right: the ***GaInP:Zn/InP:S*** configuration.

2.2 Processing and measurements

The NW morphology after growth was inspected by a Zeiss LEO 1560 field-emission scanning electron microscopy (SEM) after growth, and the material composition was characterized by a Bruker D8 X-ray diffraction equipment. A JEOL 3000F high resolution transmission electron microscopy (HRTEM) with a Scanning-TEM part and equipped with energy dispersive X-ray spectroscopy (EDX), was utilized to analyze the crystal structure and local chemical composition of different segments and heterojunctions of the NWs. For electrical measurements, NWs were mechanically transferred from the native substrate to a coordinate grid, which was defined on a degenerately doped Si substrate with a HfO_2 layer on top of a thermally-grown SiO_2 layer. Metal contacts for p- and n-type segments were defined to the corresponding ends of the NWs by electron beam lithography (EBL), after which the surface oxide of the NWs was etched by diluted buffered hydrogen fluoride ($HF:H_2O$ = 1:10) for 30 s, followed by metal evaporation and lift-off. The p-type contact material was Ti/Zn/Au (5/20/150 nm) and the n-type contact material was Ti/Au (10/150 nm). The devices were measured at room temperature on a Cascade 1100B probe station with a Keithley 4200SCS. In addition to the evaporation of metal contacts to single NWs, electron beam induced current (EBIC) characterization on one working (GaInP:Zn/InP:S) and one non-working (GaInP:Zn/InP:Sn) sample was carried out by using a nanoprobe-system from Kleindiek Nanotechnik, mounted inside a Hitachi SU8010 SEM. The samples were cleaved to access NWs (in the center) in a cross-sectional view and otherwise probed as-grown. The substrate glued to a SEM base using silver paste and a tungsten nanoprobe in direct contact with the gold seed particle, acted as back and front contacts, respectively. EBIC characterization was performed using an acceleration voltage of 5 kV, and an e-beam current in the range of tens of picoamperes (from reference measurements using a Faraday cup). The beam settings ensure low excitation conditions during EBIC scans. EBIC characterization was done for 4-5 NWs on each sample.

3. Results and discussions

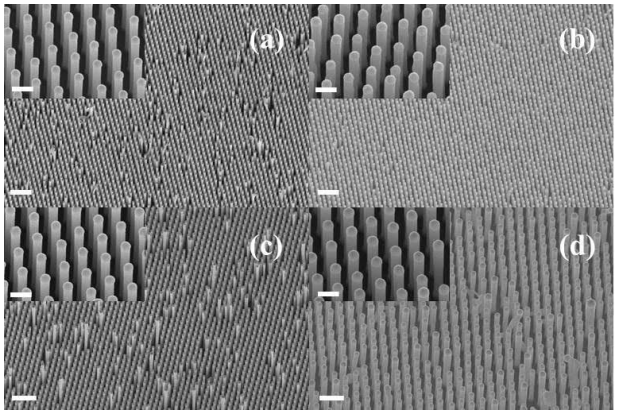

Figure 2 SEM images of InP(bottom)/GaInP(top) and GaInP(bottom)/InP(top) NW tunnel diodes, 30° tilted towards the normal of the plane, the scale bars of the images are 2 µm, and the ones of the insets are 400 nm. (a) ***InP:Sn/GaInP:Zn***; (b) ***GaInP:Zn/InP:S***; (c) InP:S/GaInP:Zn; (d) GaInP:Zn/InP:Sn.

Figure 2 shows as-grown NW tunnel diode samples of the four configurations. The average NW diameter for each sample lies within 180 ± 5 nm. A controlled growth of the NW array needs to be maintained to enable implementation into future high performing array devices. Therefore, where straight NW growth was maintained, we used the highest possible doping flows (Fig. 2), with the aim to reach degenerate doping needed for band-to-band tunneling.

A total of 12 devices were electrically contacted and measured at room temperature for each configuration. Among the four configurations, we measured current-voltage curves with Esaki diode characteristics including a negative differential resistance (NDR) region in the InP:Sn/GaInP:Zn and GaInP:Zn/InP:S configuration. I-V curves from a representative device of both configurations are

shown in Fig. 3(a) and Fig. 3(b) respectively. First, we look at the InP:Sn/GaInP:Zn configuration (Fig. 3(a)). The NDR region was observed with a relatively large variation of peak voltage between NWs (ranging from 0.3 to 2 V) which we attributed to the series resistance of the Schottky-like contact to the p-type GaInP segment [19, 29]. Under reverse bias, the poor contact explains the large breakdown voltage (~-1 V), which should ideally be close to 0 V for Zener tunneling [33]. The measured peak current varied from 0.01 to 3.9 nA between devices and the range of PVCR was from 1.1 to 2.4, both of which we argue are related to the variation of effective tunnel barrier thickness and/or defect density [19].

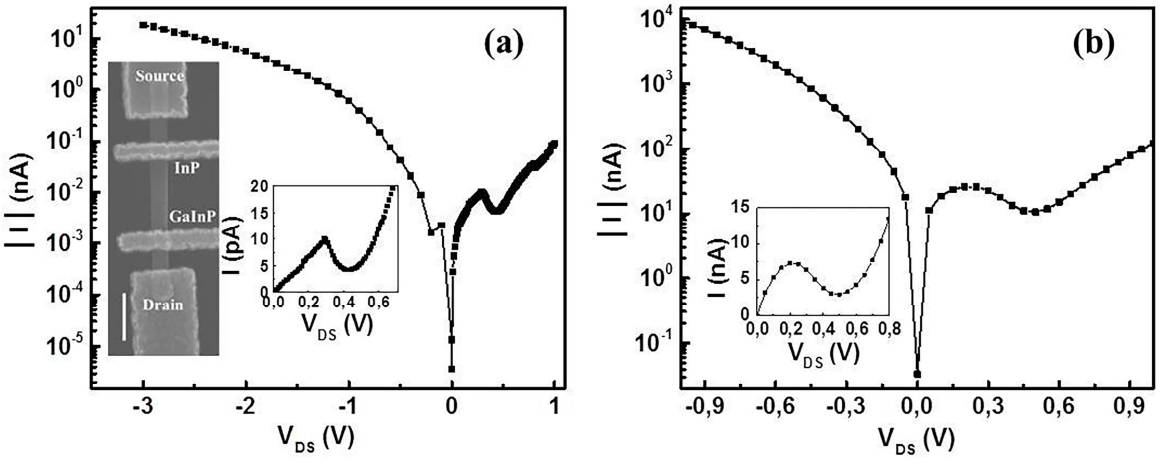

Figure 3 I-V sweep of the two working tunnel diode configurations: (a) the InP:Sn/GaInP:Zn configuration, before contact annealing since annealing dis-improved the tunnel diode characteristics; The measurement points are more frequent for positive bias in order to map out the NDR region correctly; the left inset shows the top-view SEM image of a representative contacted single NW tunnel diode, the scale bar is 500 nm; the extra perpendicular contacts on each segment were added to have the opportunity to electrically characterize each segment individually; the right inset shows the zoom-in NDR region. (b) the GaInP:Zn/InP:S configuration, after contact annealing which improved the tunnel diode characteristics; the inset shows the zoom-in NDR region.

On the one hand, the direct tunneling current T_t is exponentially dependent on the effective barrier thickness

$$T_t \approx \exp\left(\frac{-4\sqrt{2m^*}E_g^{3/2}}{3q\hbar\varepsilon}\right)\exp\left(\frac{-E_\perp\pi\sqrt{2m^*E_g}}{q\hbar\varepsilon}\right)$$

where q is the elementary charge, ħ is the reduced Planck constant, E_g is the bandgap energy, $E_\perp$ is the transverse energy of electron associated with momentum perpendicular to the direction of tunneling, m* is the effective mass, and ε is the built-in electric field of the junction [34]. The equation implies that the less abrupt the heterojunction and doping profile, the weaker the built-in electric field, thereby the smaller the tunneling current. On the other hand, the defects distributed in the depletion region of the heterojunction can dominate the peak current by affecting the resonant tunneling current [35]. Here, for the InP:Sn/GaInP:Zn configuration, it is challenging to achieve an abrupt change in doping at the InP/GaInP heterojunction since the high vapor pressure of DEZn leads to a time dependent saturation of doping after introduction of the precursor [36].

Looking next at the inverse GaInP:Zn/InP:S configuration (Fig. 3(b)), the peak current varies from 0.8 to 5.4 nA (before contact annealing). The PVCR ranges from 1.4 to 2.1. Compared with the

InP:Sn/GaInP:Zn configuration, the GaInP:Zn/InP:S configuration shows a smaller distribution of peak current and peak voltage (ranging from 0.2 to 0.35 V) between samples. We argue that the smaller distribution in this configuration is most probably because that Zn has reached its saturation limit and that S incorporates faster than Zn in the InP:Sn/GaInP:Zn configuration after the flow was switched at the heterojunction. This would result in a sharper doping transition and a higher electric field across the junction. All current-voltage curves of the InP:S/GaInP:Zn and GaInP:Zn/InP:Sn configurations presented normal diode behavior without tunneling (the I-V curves are shown in Fig. S2 in the ESM). The average break-down voltage for the devices of the InP:S/GaInP:Zn and GaInP:Zn/InP:Sn configurations are approximately -3 V and -6 V respectively.

In order to investigate the relation between material properties and electrical measurement results, TEM measurement as well as EDX scans were performed. HRTEM images (example images of the GaInP:Zn/InP:S configuration are shown in Fig. S3 in the ESM) reveal that the p-GaInP segment has zincblende (ZB) crystal structure with twin planes induced by addition of high DEZn flow, which is similar to the p-GaInP segments in the other three configurations. This is consistent with the previous reports on Zn doped InP and GaInP NWs [29, 37]. As for the n-InP segments in the four configurations, S doping induced predominately wurtzite (WZ) structure, in line with previous investigation on InP NWs [38]. No changes in NW diameter were observed, indicating minimal radial growth.

As depicted in Fig. 4, the InP/GaInP configurations (Fig. 4(a), Fig. 4(c)) have a less abrupt heterointerface than the GaInP/InP configurations (Fig. 4(b), Fig. 4(d)). A sharper Ga-In switch than In-Ga switch is explained by a higher affinity of Au for In than that for Ga; therefore the stored Ga in the seed particle is expelled and replaced more rapidly with In than vice versa [39]. Although a graded heterojunction is less favorable for tunneling, we obtained working tunnel diodes in both InP/GaInP and GaInP/InP configurations. Therefore, we argue that the dopant gradients have greater influence than the material transition on carrier tunneling.

Compared with the GaInP:Zn/InP:S configuration, the absence of tunneling current in the GaInP:Zn/InP:Sn configuration can be related to the n-type doping level in the InP segment, since the bottom GaInP:Zn segment is nominally identical in both configurations. Sn has a larger solubility in gold than S [40, 41] which could result in a delay of incorporation since the liquid catalyst alloy needs to be saturated by Sn before it precipitates. Note that we achieved a higher doping level in InP by using H_2S than TESn in our system [26, 28], suggesting that the GaInP:Zn/InP:S configuration has a larger tolerance of any doping compensation from the residual Zn in the reactor.

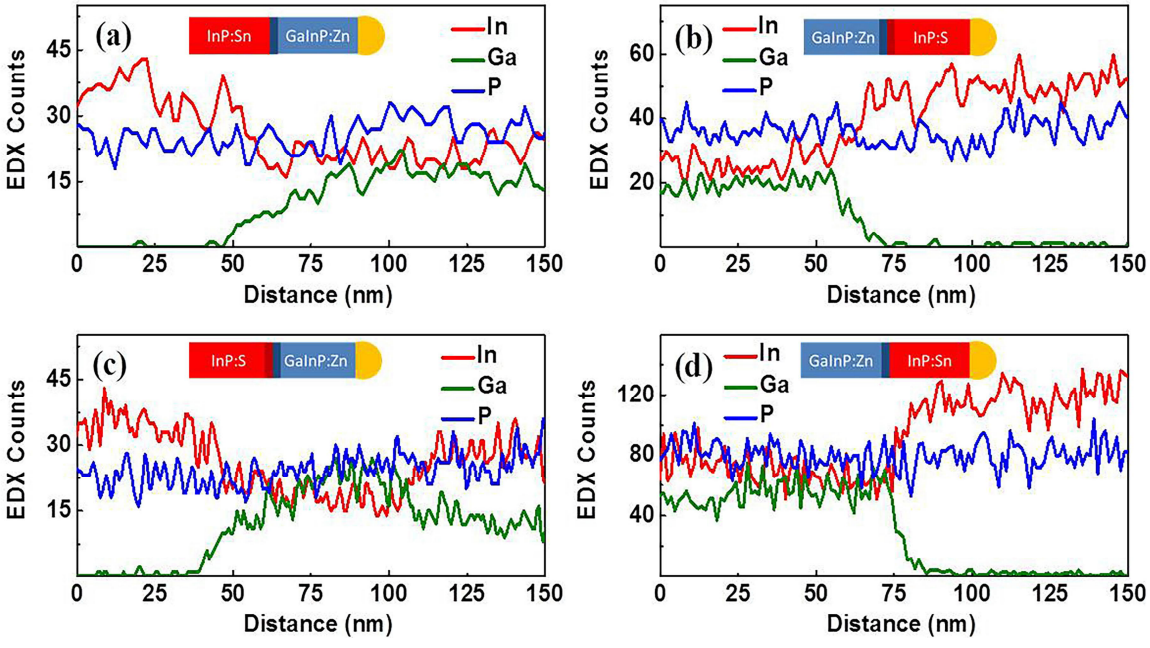

Figure 4 EDX line scans along the heterojunction of the four configurations (a) ***InP:Sn/GaInP:Zn***; (b) ***GaInP:Zn/InP:S***; (c) InP:S/GaInP:Zn; (d) GaInP:Zn/InP:Sn.

In order to improve the electrical transparency of the contacts to the nanowires, rapid thermal annealing was carried out at 350 °C for 10 s in N_2 gas atmosphere. For the sample of the GaInP:Zn/InP:S configuration, the current in the GaInP segment increased by approximately 10 times, indicating that the transparency of the contacts was improved. The peak current was improved from 5.4 nA to 7.3 nA and PVCR was improved from 2.1 to 2.5. The highest measured peak current density was 25 A/cm^2, higher than needed for state-of-the-art solar cells [42]. The total current density added within an extended area exceeds the maximum current density generated by the sun; despite any electrical contact difficulties, this is a promising result for the application in tandem junction solar cells. The same annealing conditions were applied to the other three configurations. However, the results showed degradation of I-V characteristics, consistent with the thermal load in planar tunnel diodes due to trap assisted (TAT) tunneling [43]. Other reasons could be the degradation of the heterojunction abruptness caused by interdiffusion of atoms, or doping compensation at the pn-junction interface.

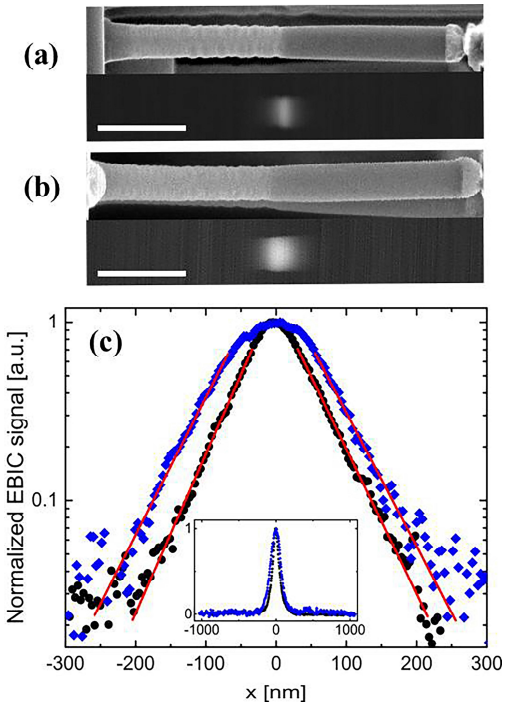

Figure 5 SEM (top) and EBIC (bottom) images of a representative NW from sample with (a) the ***GaInP:Zn/InP:S*** and (b) the GaInP:Zn/InP:Sn configuration.

The scale bars are 500 nm. (c) Normalized line scans taken from EBIC profiles in (a)-black circles, and (b)-blue diamonds, with the peaks centered at x=0. Red solid lines show exponential decay fits to extract effective minority carrier diffusion lengths. The inset shows the line scans for the full NW length, with a linear y-axis.

To gain further understanding of the characteristics of our NW heterostructure tunnel diodes, we performed EBIC characterization on a working (GaInP:Zn/InP:S) and a non-working (GaInP:Zn/InP:Sn) configuration, as shown in Fig. 5. The shape of the EBIC profiles obtained (Fig. 5(a), Fig. 5(b)) can be affected by the depletion region width of the pn-junction, the beam excitation volume, and the effective minority carrier diffusion length (a product of the bulk minority carrier diffusion length and the surface recombination velocity) on each side of the junction [44]. From line scans of the EBIC profiles (Fig. 5(c)), we first extract effective minority carrier diffusion lengths, L_{eff}, by fitting the expression $I=I_0 \times \exp(-x/L_{eff})$ to the exponentially decaying signal on each side of the junction. These fits (examples shown as solid red lines in Fig. 5(c)) gave an L_{eff} for both n- and p- regions in both configurations of between 45 and 65 nm for all measured NWs, with no significant difference between regions/configurations. As a comparison, these values for L_{eff} are somewhat below values obtained by EBIC in unpassivated GaAs NWs of similar diameter [45, 46]. Considering the generally superior surface characteristics of unpassivated InP to GaAs [47], this indicates that the found effective minority carrier diffusion length is limited by the high doping in our materials. We expect that in the NW geometry, where the surface to volume ratio is large, the effect of high doping levels on the surface recombination velocity [48, 49] will most significantly limit the effective minority carrier diffusion length. For the region close to the junction, where no exponential behavior is seen, deconvolution of the width of the depletion region and the effect of the beam excitation volume might not be straightforward. For the purpose of our discussion, however, we would like to note that the two configurations were measured under nominally identical beam conditions, and that the beam excitation volume can therefore be considered similar. Thus, the wider EBIC profile seen in the GaInP:Zn/InP:Sn configuration (Fig. 5(b)) as compared to the GaInP:Zn/InP:S configuration (Fig. 5(a)) indicates a wider depletion region in the non-working configuration.

4. Conclusions

We have grown NW tunnel diodes in the InP/GaInP and GaInP/InP configurations using a material system for optimal light absorption in a tandem junction geometry. Electrical measurements showed tunnel diode characteristics with maximum peak current density of 25 A/cm^2, PVCR up to 2.5. This work shows that InP/GaInP nanowire tunnel diodes can be realized independently of the order of growth of the different materials, offering flexibility in doping polarity for the optimization of the device performance. The InP:Sn/GaInP:Zn and GaInP:Zn/InP:S configurations showed efficient tunnel junction behavior, whereas the InP:S/GaInP:Zn and GaInP:Zn/InP:Sn configurations were found to be less favorable for carrier tunneling, possibly because of Zn concentration saturation delay, and carry-over effect of Sn, dissolved in the liquid metal particle utilized for growth. Further, by comparing EBIC profiles of a working and a non-working configuration, we can confirm a wider depletion region for the non-working configuration. Our results demonstrate new material combinations for tunnel diodes, and the reveal the suitability of

different dopant species with respect to the growth of nanowire tunnel diodes in InP/GaInP material systems that are suitable for nanowire tandem solar cells.

Acknowledgements

We thank Dr. Enrique Barrigón and Dr. Pyry Kivisaari for helpful discussions during the course of this work. We also thank Dr. Ingvar Åberg and co-workers at SolVoltaics AB, for help with EBIC measurements. The research leading to these results was performed within NanoLund at Lund University and supported by the Crafoord Foundation, the Swedish Research Council, the Swedish Energy Agency, the Coordination for the Improvement of Higher Education Personnel (CAPES-Brazil), the European Union's Horizon 2020 research and innovation programme under grant agreement No°641023 (Nano-Tandem), and the People Programme (Marie Curie Actions) of the European Union's Seventh Framework Programme (FP7-People-2013-ITN) under REA grant agreement No°608153, PhD4Energy. This publication reflects only the author's views and the funding agency is not responsible for any use that may be made of the information it contains.

Electronic Supplementary Material: Electrical measurements on non-working configurations. TEM and EDX measurement on the NW with the GaInP:Zn/InP:S configuration. The supplementary material is available in the online version of this article at http://dx.doi.org/10.1007/s12274-***-****-*.

References

[1] Hiruma, K.; Katsuyama, T.; Ogawa, K.; Koguchi, M.; Kakibayashi, H. Quantum size microcrystals grown using organometallic vapor phase epitaxy. *Appl. Phys. Lett*. **1991**, *59* (4), 431-433.

[2] Gudiksen, M. S.; Lauhon, L. J.; Wang, J.; Smith, D. C.; Lieber, C. M. Growth of nanowire superlattice structures for nanoscale photonics and electronics. *Nature* **2002**, *415*, 617-620.

[3] Samuelson, L.; Björk, M. T.; Deppert, K.; Larsson, M.; Ohlsson, B. J.; Panev, N.; Persson, A. I.; Sköld, N.; Thelander, C.; Wallenberg, L. R. Semiconductor nanowires for novel one-dimensional devices. *Physica E* **2004**, *21*, 560-567.

[4] Heurlin, M.; Magnusson, M. H.; Lindgren, D.; Ek, M.; Wallenberg, L. R.; Deppert, K.; Samuelson, L. Continuous gas-phase synthesis of nanowires with tunable properties. *Nature* **2012**, *492*, 90-94.

[5] Anttu, N.; Xu, H. Q. Coupling of light into nanowire arrays and subsequent absorption. *J. Nanosci. Nanotechno.* **2010**, *10*, 7183-7187.

[6] Borgström, M. T.; Wallentin, J.; Heurlin, M.; Fält, S.; Wickert, P.; Leene, J.; Magnusson, M. H.; Deppert, K.; Samuelson, L. Nanowires with promise for photovoltaics. *IEEE J. Sel. Top. Appl.* **2011**, *17*, 1050-1061.

[7] Otnes, G.; Borgström, M. T. Towards high efficiency nanowire solar cells. *Nanotoday* **2017**, 12, 31–45

[8] Wallentin, J.; Anttu, N.; Asoli, D.; Huffman, M.; Åberg, I.; Magnusson, M. H.; Siefer, G.; Fuss-Kailuweit, P.; Dimroth, F.; Witzigmann, B.; Xu, H. Q.; Samuelson, L.; Deppert, K.; Borgström, M. T. InP nanowire array solar cells achieving 13.8% efficiency by exceeding the ray optics limit. *Science* **2013**, *339* (6123**)**, 1057-1060.

[9] Åberg, I.; Vescovi, G.; Asoli, D.; Naseem, U.; Gilboy, J. P.; Sundvall, C.; Dahlgren, A.; Svensson, K. E.; Anttu, N.; Björk, M. T.; Samuelson, L. A GaAs nanowire array solar cell with 15.3% efficiency at 1 sun. *IEEE J. Photovolt*. **2015**, *6*, 185-190.

[10] van Dam, D.; van Hoof, N. J. J.; Cui, Y.; van Veldhoven, P. J.; Bakkers, E. P. A. M.; Rivas, J. G.; Haverkort, J. E. M. High-efficiency nanowire solar cells with omnidirectionally enhanced absorption due to self-aligned Indium-Tin-Oxide Mie scatterers. *ACS Nano*. **2016**, *10*, 11414-11419.

[11] LaPierre, R. R.; Chia, A. C. E.; Gibson, S. J.; Haapamaki, C. M.; Boulanger, J.; Yee, R.; Kuyanov, P.; Zhang, J.; Tajik, N.; Jewell, N. et al. III–V nanowire photovoltaics: Review of design for high efficiency. *Phys. Status Solidi RRL* **2013**, 7, 815–830.

[12] Heurlin, M.; Wickert, P.; Fält, S.; Borgström, M. T.; Deppert, K.; Samuelson, L.; Magusson, M. H. Axial InP nanowire tandem junction grown on a silicon substrate. *Nano Lett.* **2011**, *11*, 2028-2031.

[13] Kempa, T. J.; Tian, B.; Kim, D. R.; Hu, J.; Zheng, X.; Lieber, C. M. Single and tandem axial p-i-n nanowire photovoltaic devices. *Nano Lett.* **2008**, *8* (10), 3456-3460.

[14] Yao, M.; Cong, S.; Arab, S.; Huang, N.; Povinelli, M. L.; Cronin, S. B.; Dapkus, P. D.; Zhou, C. Tandem solar cells using GaAs nanowires on Si: design, fabrication, and observation of voltage addition. *Nano Lett.* **2015**, *15* (11), 7217-7224.

[15] Dimroth, F. High-efficiency solar cells from III-V compound semiconductors. *Phys. Stat. Sol. (c)* **2006**, *3* (3), 373-379.

[16] Chen, Y.; Pistol, M.-E.; Anttu, N. Design for strong absorption in a nanowire array tandem solar cell. *Sci. Rep.* **2016**, *6*, 32349.

[17] Esaki, L. New phenomenon in narrow Germanium p-n junctions. *Phys. Rev.* **1958**, *109* (2), 603-604.

[18] Luque, A.; Hegedus, S. *Handbook of Photovoltaic Science and Engineering;* John Wiley & Sons, Ltd.: Chichester, 2011.

[19] Wallentin, J.; Persson, J. M.; Wagner, J. B.; Samuelson, L.; Deppert, K.; Borgström, M. T. High-performance single nanowire tunnel diodes. *Nano Lett.* **2010**, *10*, 974-979.

[20] Borg, B. M.; Dick, K. A.; Ganjipour, B.; Pistol, M.-E.; Wernersson, L.-E.; Thelander, C. InAs/GaSb heterostructure nanowires for tunnel field-effect transistors. *Nano Lett.* **2010**, *10*, 4080-4085.

[21] Schmid, H.; Bessire, C.; Björk, M. T.; Schenk, A.; Riel, H. Silicon nanowire Esaki diodes. *Nano Lett.* **2012**, *12*, 699-703.

[22] Ganjipour, B.; Dey, A. W.; Borg, B. M.; Ek, M.; Pistol, M.-E.; Dick, K. A.; Wernersson, L.-E.; Thelander, C. High current density Esaki tunnel diodes based on GaSb-InAsSb heterostructure nanowires. *Nano Lett.* **2011**, *11*, 4222-4226.

[23] Fung, W. Y.; Chen, L.; Lu, W. Esaki tunnel diodes based on vertical Si-Ge nanowire heterojunctions. *Appl. Phys. Lett*. **2011**, *99*, 092108.

[24] Nadar, S.; Rolland, C.; Lampin, J.-F.; Wallart, X.; Caroff, P.; Leturcq, R. Tunnel junctions in a III–V nanowire by surface engineering. *Nano Res.* **2015**, *8* (3), 980-989.

[25] Otnes, G.; Heurlin, M.; Graczyk, M.; Wallentin, J.; Jacobsson, D.; Berg, A.; Maximov, I.; Borgström, M. T. Strategies to obtain pattern fidelity in nanowire growth from large-area surfaces patterned using nanoimprint lithography. *Nano Res*. **2016**, *9* (10), 2852-2861.

[26] Hultin, O.; Otnes, G.; Borgström, M. T.; Björk, M.; Samuelson, L.; Storm, K. Comparing Hall effect and field effect measurements on the same single nanowire. *Nano Lett.* **2016**, *16* (1), 205-211.

[27] Borgstöm, M. T.; Norberg, E.; Wickert, P.; Nilsson, H. A.; Trägårdh, J.; Dick, K. A.; Statkute, G.; Ramvall, P.; Deppert, K.; Samuelson, L. Precursor evaluation for in situ InP nanowire doping. *Nanotechnology* **2008**, *19*, 445602.

[28] Lindelöw, F.; Heurlin, M.; Otnes, G.; Dagytė, V.; Lindgren, D.; Hultin, O.; Storm, K.; Samuelson, L.; Borgström, M. T. Doping evaluation of InP nanowires for tandem junction solar cells. *Nanotechnology* **2016**, *27*, 065706.

[29] Otnes, G.; Heurlin, M.; Zeng, X.; Borgström, M. T. $In_xGa_{1-x}P$ Nanowire growth dynamics strongly affected by doping using Diethylzinc. *Nano Lett.* **2017**, *17* (2), 702-707.

[30] Heurlin, M.; Anttu, N.; Camus, C.; Samuelson, L.; Borgström, M. T. In situ characterization of nanowire dimensions and growth dynamics by optical reflectance. *Nano Lett.* **2015**, *15*, 3597-3602.

[31] Borgström, M. T.; Wallentin, J.; Trägårdh, J.; Ramvall, P.; Ek, M.; Wallenberg, L. R. In situ etching for total control over axial and radial nanowire growth. *Nano Res.* **2010**, *3* (4), 264-270.

[32] Jacobsson, D.; Persson, J. M.; Kriegner, D.; Etzelstorfer, T.; Wallentin, J.; Wagner, J. B.; Stangl, J.; Samuelson, L.; Deppert, K.; Borgström, M. T. Particle-assisted $Ga_xIn_{(1-x)}P$ nanowire growth for designed bandgap structures. *Nanotechnology* **2012**, *23*, 245601.

[33] Zener, C. A theory of the electrical breakdown of solid dielectrics. In *Proceedings of the Royal Society of London*, London, UK, **1934**, pp 523-529.

[34] Sze, S. M.; Ng, K. K. *Physics of Semiconductor Devices*; John Wiley & Sons Inc.: Hoboken, **2007**.

[35] Jandieri, K.; Baranovskii, S. D.; Rubel, O.; Stolz, W.; Gebhard, F.; Guter, W.; Hermle, M.; Bett, A. W. Resonant electron tunnelling through defects in GaAs tunnel diodes. *J. Appl. Phys.* **2008**, *104* (9), 094506.

[36] Gutsche, C.; Regolin, I.; Blekker, K.; Lysov, A.; Prost, W.; Tegude, F. J. Controllable p-type doping of GaAs nanowires during vapor-liquid-solid growth. *J. Appl. Phys.* **2009**, *105* (2), 024305.

[37] Algra, R. E.; Verheijen, M. A.; Borgström, M. T.; Feiner, L.-F.; Immink, G.; van Enckevort, W. J. P.; Bakkers, E. P. A. M. Twinning superlattices in indium phosphide nanowires. *Nature* **2008**, *456*, 369-372.

[38] van Weert, M. H. M.; Helman, A.; can den Einden, W.; Algra, R. E.; Verheijen, M. A.; Borgström, M. T.; Immink, G.; Kelly, J. J.; Kouwenhoven, L. P.; Bakkers, E. P. A. M. Zinc incorporation via the vapor-liquid-solid mechanism into InP nanowires. *J. Am. Chem. Soc.* **2009**, *131* (13), 4578-4579.

[39] Dick, K. A.; Bolinsson, J.; Borg, B. M.; Johansson, J. Controlling the abruptness of axial heterojunctions in III-V nanowires: beyond the reservoir effect. *Nano Lett.* **2012**, *12*, 3200-3206.

[40] Okamoto, H.; Massalski, T. B. The Au-S (gold-sulfur) system. *Bull. Alloy Phase Diagr.* **1985**, *6*, 518-519.

[41] Ciulik, J.; Notis, M. R. The Au-Sn phase diagram. *J. Alloy Compd.* ***1993****, 191*, 71-78.

[42] Guter, W.; Schone, J.; Philipps, S. P.; Steiner, M.; Siefer, G.; Wekkli, A.; Welser, E.; Oliva, E.; Bett, A. W.; Dimroth, F. Current-matched triple-junction solar cell reaching 41.1% conversion efficiency under concentrated sunlight. *Appl. Phys. Lett.* **2009**, *94* (22), 223504.

[43] Barrigón, E.; García, I.; Barrutia, L.; Rey-Stolle, I.; Algora, C. Highly conductive p^{++}-AlGaAs/n^{++}-GaInP tunnel junctions for ultra-high concentrator solar cells. *Prog. Photovolt: Res. Appl.* **2014**, *22*, 399-404.

[44] Leamy, H. J. J. Charge collection scanning electron microscopy. *Appl. Phys.* **1982**, *53*, R51-R80.

[45] Gutsche, C.; Niepelt, R.; Gnauck, M.; Lysov, A.; Prost, W.; Ronning, C.; Tegude, F. J. Direct determination of minority carrier diffusion lengths at axial GaAs nanowire p-n junctions. *Nano Lett.* **2012**, *12*, 1453-1458.

[46] Darbandi, A.; Watkins, S. P. Measurement of minority carrier diffusion lengths in GaAs nanowires by a nanoprobe technique. *J. Appl. Phys.* **2016**, *120*, 014301.

[47] Joyce, H. J.; Docherty, C. J.; Gao, Q.; Tan, H. H.; Jagadish, C.; Lloyd-Hughes, J.; Herz, L. M.; Johnston, M. B. Electronic properties of GaAs, InAs and InP nanowires studied by terahertz spectroscopy. *Nanotechnology* **2013**, *24*, 214006.

[48] Aspnes, D. E. Recombination at semiconductor surfaces and interfaces. *Surf Sci.* **1983**, *132*, 406-421.

[49] Bothra, S.; Tyagi, S.; Ghandhi, S. K.; Borrego, J. M. Surface recombination velocity and lifetime in InP. *Solid State Electron.* **1991**, *34*, 47-50.